International Forum on Aeroelasticity and Structural Dynamics
IFASD 2024
17-21 June 2024, The Hague, The Netherlands

TRANSONIC LIMIT CYCLE OSCILLATIONS OF THE BENCHMARK SUPERCRITICAL WING

Bret Stanford[1], **Pawel Chwalowski**[1], **Kevin Jacobson**[1]

[1]NASA Langley Research Center
Hampton, VA, 23681
bret.k.stanford@nasa.gov
pawel.chwalowski@nasa.gov
kevin.e.jacobson@nasa.gov

Keywords: transonic flow, flutter, limit cycle oscillations

Abstract: This paper considers transonic flutter mechanisms of the Benchmark Supercritical Wing, a model under study in the Aeroelastic Prediction Workshop series. Flutter boundaries are mapped out across an angle-of-attack sweep at Mach 0.8, utilizing both time-domain and linearized frequency-domain solvers, manual meshes and adapted meshes, and various governing equations. With increased angle-of-attack, linearized and finite amplitude flutter predictions exhibit differences above 3° as the flow begins to separate; the latter predictions are found to be driven by subcritical limit cycle oscillations whose strength increases with angle-of-attack. Moderate perturbation values provide a stability boundary at 5° that matches the experimental data, but it is not clear how the experimental perturbation, from one test condition to the next, can be reasonably characterized.

1 INTRODUCTION

Transonic aeroelastic flutter will be a key design driver for future transport aircraft, owing to trends of higher wingspans and thinner wings, driven by a need for reduced fuel burn. Industry accepted aeroelastic solvers rely on linear aerodynamics with steady transonic corrections (usually derived from wind tunnel testing): CFD-based predictions are typically viewed as overly expensive and nonrobust. However, a true accounting of transonic flutter for nontraditional aircraft concepts will, likely, require accurate CFD-based computations, to properly handle unsteady aeroelastic mechanisms driven by strong aerodynamic nonlinearities [1,2]. A key barrier to the development of inexpensive and robust transonic aeroelastic prediction tools, is the relative scarcity of experimental benchmarking data.

One candidate dataset is that of the Benchmark Supercritical Wing (BSCW), an aeroelastic configuration tested in the NASA Langley Transonic Dynamics Tunnel (TDT) in 1992 [3]. This model consists of a nominally rigid unswept rectangular wing (16” chord, 32” semispan) with a constant supercritical airfoil, attached at its root to a two-degree-of-freedom pitch and plunge apparatus (PAPA). This configuration was a focus of the first three Aeroelastic Prediction Workshops (AePW), the last of which took place in January of 2023*. The transonic flutter condition considered in AePW-3 was at Mach 0.8, 5° angle-of-attack (AoA): this case consists of large regions of separated flow over the wing and is therefore very challenging for modern computational aeroelastic solvers.

*https://nescacademy.nasa.gov/workshops/AePW3/public/

A comparison of results across the various AePW-3 participants [4] showed large variations in the flutter boundary, due in part to the fact that the flutter mechanism is relatively weak, with a shallow crossing of the aeroelastic eigenvalue with increasing dynamic pressure. As such, nominally minor differences in aeroelastic software settings or configuration setup could lead to large variations in the computed instability boundary. Furthermore, previous work by the authors [5] has noted that the flutter point at the Mach 0.8, 5° AoA case is heavily dependent on the perturbation size. After a static aeroelastic equilibrium solution is computed, a modal perturbation is applied to the system in the form of a generalized velocity applied to both the pitch and plunge modes. The resulting dynamic aeroelastic damping is dependent on that perturbation size: this dependency also hinders comparisons across the AePW-3 participants, since perturbation size had not been a specified test case input. Some participants did not apply a perturbation at all, but instead began the dynamic aeroelastic simulation directly from the flow condition about the rigid wing.

The focus of this paper is to better understand and demonstrate the dependency of the flutter mechanism upon the perturbation size, which manifests itself in the form of a large subcritical limit cycle oscillation (LCO). The analysis is performed not only for the AePW condition of 5° AoA, but at a range of AoA values, to better understand the onset of strong flow nonlinearities. Aeroelastic solvers built into the FUN3D [6] software are used for this exercise, including both time-domain and frequency-domain predictions, conducted on both manually generated meshes and automatically adapted meshes.

2 MODEL AND TEST DESCRIPTION

The BSCW model has an unswept untapered rectangular planform with a 16” chord and a 32” semispan, and a NASA SC(2)-0414 airfoil. The wing itself is nominally rigid but is attached at its root to a pitch and plunge apparatus (PAPA), which provides the two structural degrees of freedom. The PAPA mechanism consists of four circular cross section bars and a central drag strut. When the BSCW model is attached to the PAPA mechanism, the rigid body plunge frequency of the system is 3.33 Hz, and the rigid body pitch frequency is 5.20 Hz. In addition, the model is mounted to a large splitter plate (as seen in Fig. 1), in order to offset the wing by 40” from the thick boundary layer of the tunnel wall.

The BSCW model is outfitted with numerous thermocouples, accelerometers, and pressure transducers, but only the actual flutter points of the original TDT test [7] (in terms of dynamic pressure, q, at a given Mach and AoA value) are utilized for this work. This data is taken in an R-12 test medium, which has a speed of sound of 505 ft/s (nearly half the value found in air), and is conducted with a #35 grit transition strip at the 6.5% chord line.

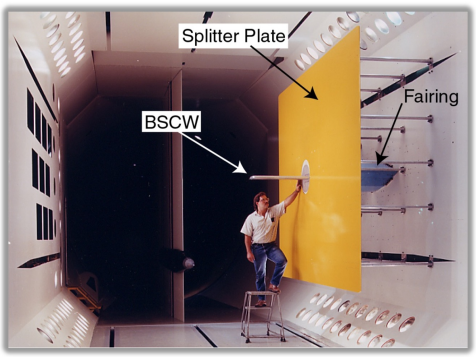

Figure 1: Photograph of the BSCW mounted to the splitter plate and PAPA mechanism [source: NASA].

3 COMPUTATIONAL METHODS

All simulations are performed within FUN3D, an unstructured flow solver [6]. Multiple distinct aeroelastic solver options have been used here to obtain results, and these options are summarized below. For all simulations, the splitter plate at the wing root is modeled as a symmetry plane.

3.1 Time-domain Simulations

Aeroelastic analysis in the time domain is conducted by coupling unsteady node-centered finite volume FUN3D computations to a modal structural solver integrated within FUN3D [8]. Multiple subiterations are conducted at each time step to converge the unsteady flow equations, but information between fluid and structure is only transferred once via a predictor/corrector algorithm, before moving to the next time step. Volume mesh deformation in response to surface movement is done with a linear elasticity analogy [9]. The governing equations most commonly used for this work are the unsteady Reynolds-averaged Navier-Stokes (URANS) equations, with turbulence closure obtained with the Spalart Allmaras (SA) one equation model, though some results are also obtained with Delayed Detached Eddy Simulation (DDES). [10].

Time-domain aeroelastic analysis is typically done with a three step process. First, the steady flow equations are converged over the rigid wing surface. Second, a static aeroelastic computation is obtained, by time integrating the coupled equations with modal dampings set to large values. Finally a dynamic aeroelastic solution is obtained by perturbing the modal parameters about the converged static aeroelastic solution. The perturbation is given as a generalized modal velocity, v, applied equally to both the pitch and the plunge mode; as noted above, the dependence of the aeroelastic response upon the magnitude of v is a key theme of this paper.

Alternatively, the dynamic aeroelastic equations may be started directly from the steady flow over the rigid wing, and no v perturbation is needed to instigate the dynamics. This option is termed here the "jig shape release" method. For either method, the damping and frequency of the response is estimated from the matrix pencil scheme [11]. This method assumes a linear damped oscillatory response, whereas the response of these aeroelastic systems may be nonlinear (i.e., damping will vary in time). A sliding window scheme [12] within the matrix pencil method is used to estimate the relationship between amplitude (v) and damping.

If it is desired to compute the actual flutter-q (as opposed to just the damping characteristics at a given q), the entire process given above must be repeated for increasing values of q, until an oscillatory growth is observed in the modal response. Flutter-q is finally bracketed by the final two simulations.

Given the importance of the perturbation size, v, that will be shown below, it is unclear how to estimate the size and character of the perturbation seen in the actual TDT test, as this depends on the way in which Mach and q are varied from one test point to the next, as well as local turbulence fluctuations in the test section.

All time-domain simulations in this work are conducted on a manually constructed family of grids shown in Fig. 2: a coarse 3 million node mesh, a medium 9 million node mesh, a fine 27 million node mesh, and an extra fine 99 million node mesh.

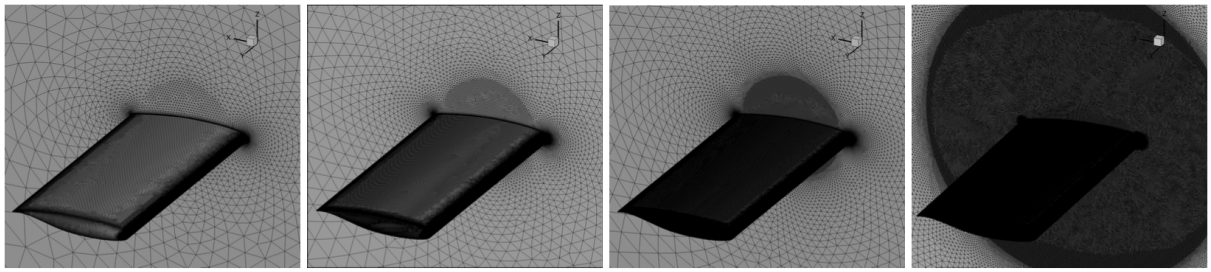

Figure 2: Manually constructed family of meshes.

3.2 Linearized Frequency-domain Simulations

Aeroelastic simulations have also been obtained with the linearized frequency-domain (LFD) method, recently implemented [13] within the stabilized finite element (SFE) [14] version of the FUN3D. LFD linearizes about a steady background flow (either flow over the rigid wing, or more accurately, flow over the static aeroelastic configuration) via infinitesimal oscillatory perturbations of each mode shape, resulting in a complex-valued set of generalized aerodynamic forces (GAFs). The GAFs are computed at a predefined list of reduced frequencies, requiring a complex-valued linear solve for each mode-frequency pair. These GAFs may then be used to directly compute flutter in a $p-k$ eigenequation [15], and the aeroelastic mode, damping, and frequency may be constructed at a range of q values.

For transonic flows, a potentially important aspect of the LFD simulations is matched point dynamic pressures. The $p-k$ solver provides aeroelastic information at a range of q values, but the only q value that is truly matched point is the value utilized for the original static aeroelastic equilibrium. An iterative process may be used to ensure the dynamic pressures are matched point: different static aeroelastic q values may cause the wing to pitch to different angles, shift the shock to a different location, and finally result in a shift in the flutter dynamic response. However, with one exception (which will be detailed below), this relationship is ignored here.

Finally, it may be expected that the aeroelastic response computed with LFD will coincide with the aeroelastic response computed via time-domain tools, as long as v is very small, since LFD assumes an infinitesimal perturbation. This will generally be shown to be true below, notwithstanding the fact that the time-domain tools use a finite volume solver, and LFD uses an SFE solver; the differences between these two solvers should diminish with finer meshes.

3.2.1 Mesh Adaptation

LFD simulations are conducted on the same family of manually constructed meshes shown in Fig. 2, but have also been implemented into an automated mesh adaptation process. Time-domain flutter simulations can also be done with mesh adaptation (see. Ref. [16] for both URANS and DDES results), but these are less tractable owing to the high computational cost of time-domain methods and are not conducted here. Mesh adaptation mechanics are handled with a sketch-to-solution workflow [17,18], specifically the *refine*[†] tool. The adaptations reduce spatial interpolation error in the flow field based on some multiscale metric [19] scalar field; the Mach number is chosen in this work. For unsteady simulations, the fixed point multiscale metric [20] is computed as an average of the Mach interpolation error tensor sampled at regular intervals of the unsteady simulation. For LFD, flow snapshots are constructed using a harmonic perturbation.

[†]Available via `https://github.com/NASA/refine`, last accessed June, 2021.

The LFD-based mesh adaptation proceeds as follows:

1. For a given AoA and a given BSCW mesh, the FUN3D/SFE tool is used to compute the steady flow around the wing.
2. The LFD solver is used to compute the GAFs, and the $p-k$ solver is then used to compute the flutter-q.
3. Using the pitch/plunge flutter eigenmode, the complex-valued flutter flow field is computed. A time history of oscillatory snapshots is constructed via a perturbation expansion: $M = M_0 + real(\delta \cdot \overline{M} \cdot e^{i \cdot \omega \cdot t})$, where M_0 is the steady Mach number field and $\overline{M}$ is the complex-valued flutter flow field. This step requires the selection of a perturbation level δ and the number of snapshots across a single oscillation.
4. With these snapshots, *refine* constructs the multiscale metric and then creates a new mesh with its adaptation mechanics.
5. The steady pitching moment about the elastic axis (midchord, for the BSCW), the flutter-q, and the pitch stiffness are used to compute the rotation needed to bring the system into pitch equilibrium. The AoA is updated as the sum of the fixed (set) AoA and this pitch rotation.
6. The process repeats back to step 1, with the new mesh and the new AoA.

The last two steps in the above process represent a loosely coupled approach to static aeroelasticity, where the static aeroelastic pitch rotation converges alongside the mesh refinement process. This accounts for the dynamic pressure matched point mechanics discussed above.

4 AePW SUMMARY

A summary of recent BSCW flutter results obtained via AePW is shown in Fig. 3, set against the backdrop of the TDT experimental envelope (solid black lines). The data points represent TDT results, and the vertical variation bars represent the range of flutter predictions computed by the workshop participants. A linear analysis, via doublet lattice method (DLM) aerodynamics, shows a slight rise in the flutter boundary with increased Mach number. Two Mach numbers were considered for flutter predictions in the second workshop[‡]: a relatively benign case at Mach 0.74, 0° AoA, and a much more challenging case at Mach 0.85, 5° AoA. The Mach 0.74 case is well predicted by the participants (this result aligns well with the linear prediction also); the blind test case at Mach 0.85, which is driven by very strong aerodynamic nonlinearities, shows a large range in flutter-q predictions.

For the third workshop, a lower transonic Mach number of 0.8 was considered, one for which three data points exist, each roughly at 5° AoA. The variation in flutter results is again large, but not as extreme as the variations seen at Mach 0.85. The damping of the critical aeroelastic mode at Mach 0.8, 5° AoA, is shown in Fig. 4, for each of the workshop participants. For this plot, a negative damping value is unstable: some of the results in the figure are unstable for all q values, and as such the minimum bound on flutter-q in Fig. 3 is 0. A similar plot is shown in Fig. 5, summarizing the frequency migration results across the workshop participants.

Beyond the fact that the transonic test case considered here is characterized by separated flow (and thus very difficult for aeroelastic solvers to predict), the flutter mechanism is a "soft" flutter mechanism with weak damping and is therefore perhaps more susceptible to solver, spatial, and temporal uncertainties, than would be found for a "hard" flutter mechanism. In addition, the

[‡]https://nescacademy.nasa.gov/workshops/AePW2/public/

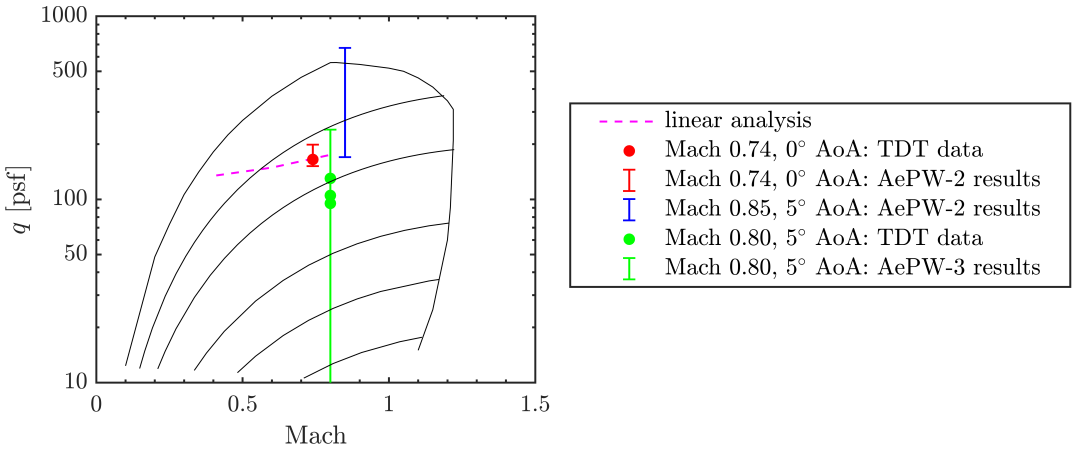

Figure 3: A summary of BSCW flutter results from AePW-2 and -3.

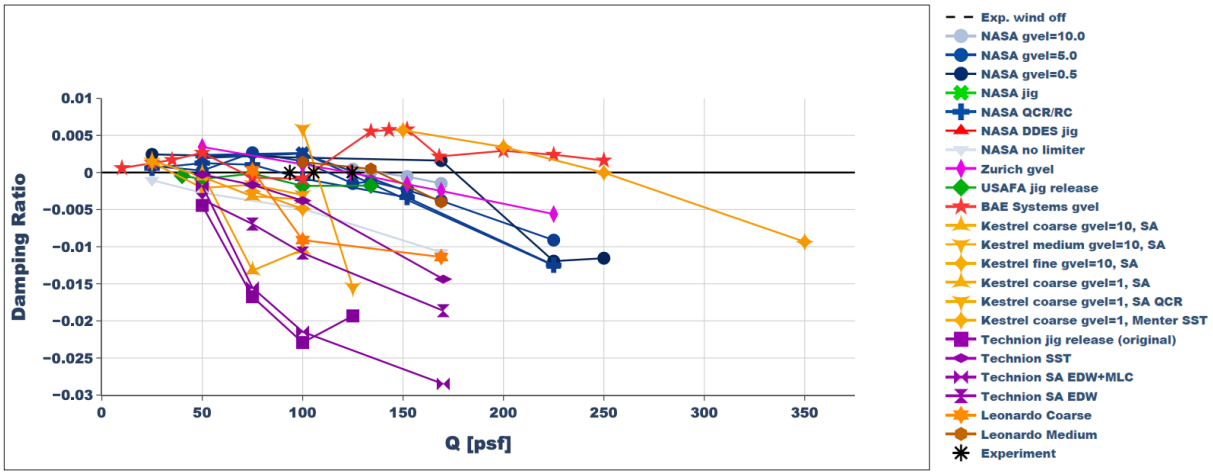

Figure 4: A summary of aeroelastic damping migration results from AePW-3.

time-domain flutter solutions are highly sensitive to the perturbation size, v, (labeled as "gvel" in the figure legend, for "generalized modal velocity"), though there is no consistent relationship between v and the flutter mechanism, across the workshop participants (for participants that varied v at all).

Additional information pertaining to Fig. 4 and Fig. 5 may be found in Ref. [4].

5 RESULTS

The remainder of this paper will consider an entire AoA sweep at Mach 0.8 (rather than a sole focus at 5° AoA), as an attempt to better understand the onset and impact of transonic flow as AoA is increased. In addition to the 5° data summarized in Fig. 3 and Fig. 4, TDT data also exists [7] at 0° and 1° AoA. First LFD-based mesh adaptation results are shown across the AoA-sweep in Fig. 6, in terms of the flutter-q and the static aeroelastic twist during the refinement process. AoA values of 0°, 1°, and 2° are all well converged with a relatively small mesh size of 10^5 nodes, while AoA's of 3° and 4° require meshes closer to 10^6 nodes.

The 5° value never truly converges with increased mesh size; many of the meshes return a

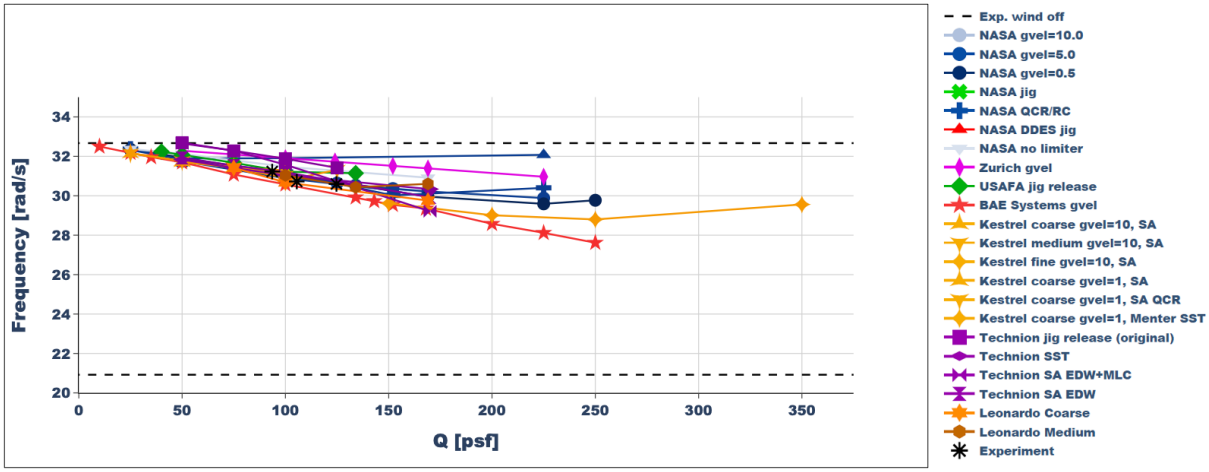

Figure 5: A summary of aeroelastic frequency migration results from AePW-3.

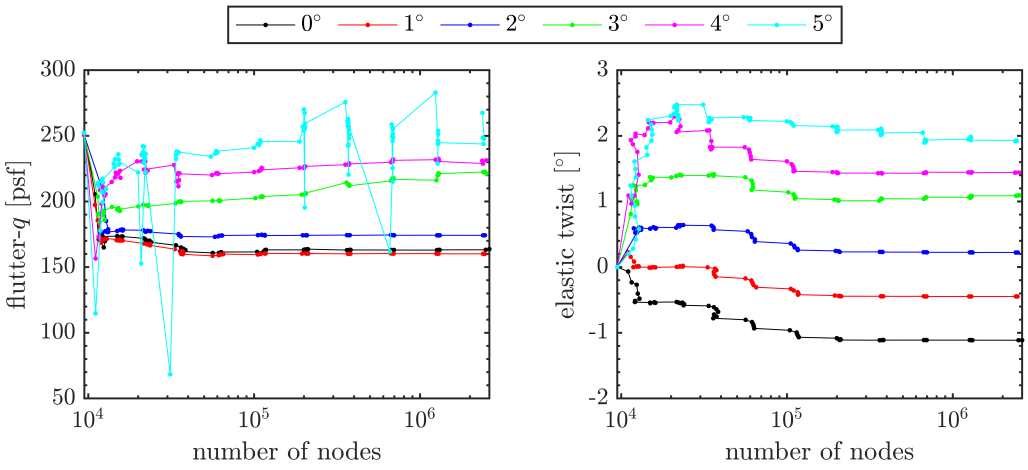

Figure 6: Convergence history of the LFD-based mesh refinement process.

flutter-q near 250 psf, but some meshes return outlier flutter values. The static aeroelastic twist at 5° AoA does converge well with mesh density, suggesting that the q matched point requirement used here is a weak driver of the transonic physics (otherwise, the static twist would also be poorly converged with mesh density). It can also be seen that static twist increases monotonically with AoA: due to the camber of the airfoil, the wing twists nose downwards at small AoA, but upwards for larger values.

Steady pressure coefficient distributions over the static aeroelastic deformed wing are shown in Fig. 7 for the six AoA conditions, and Mach contours are shown in Fig. 8 along the symmetry plane of the wing. These contours are provided for the final mesh in the adaptation process of Fig. 6. There is a weak shock along the lower surface of the wing, which dissipates as the AoA is increased. There is another shock on the upper surface of the wing, which becomes very strong with increased AoA, and it can be seen that the mesh adaptation process affords a highly resolved shock boundary above the wing surface.

At 3° AoA, the flow is mildly separated at the foot of the shock, between relative span stations of 0 and 50%. Outboard of this point, the shock weakens and shifts toward the leading edge, and the flow is attached. At 4° and 5° AoA, the shock along the symmetry plane shifts forward

but remains near the midchord further outboard. The flow at the foot of this shock is massively separated, clearly seen in Fig. 8; it is unlikely that the URANS solver used here is properly capturing the flow features at these large AoA values. Furthermore, the symmetry plane condition at the wing root is erroneous, as the root of the wing is in fact immersed in the boundary layer of the splitter plate. This assumption may impact all of the flow features seen in Fig. 7 and Fig. 8, but have a particular influence on the flow separation at 4° and 5° AoA.

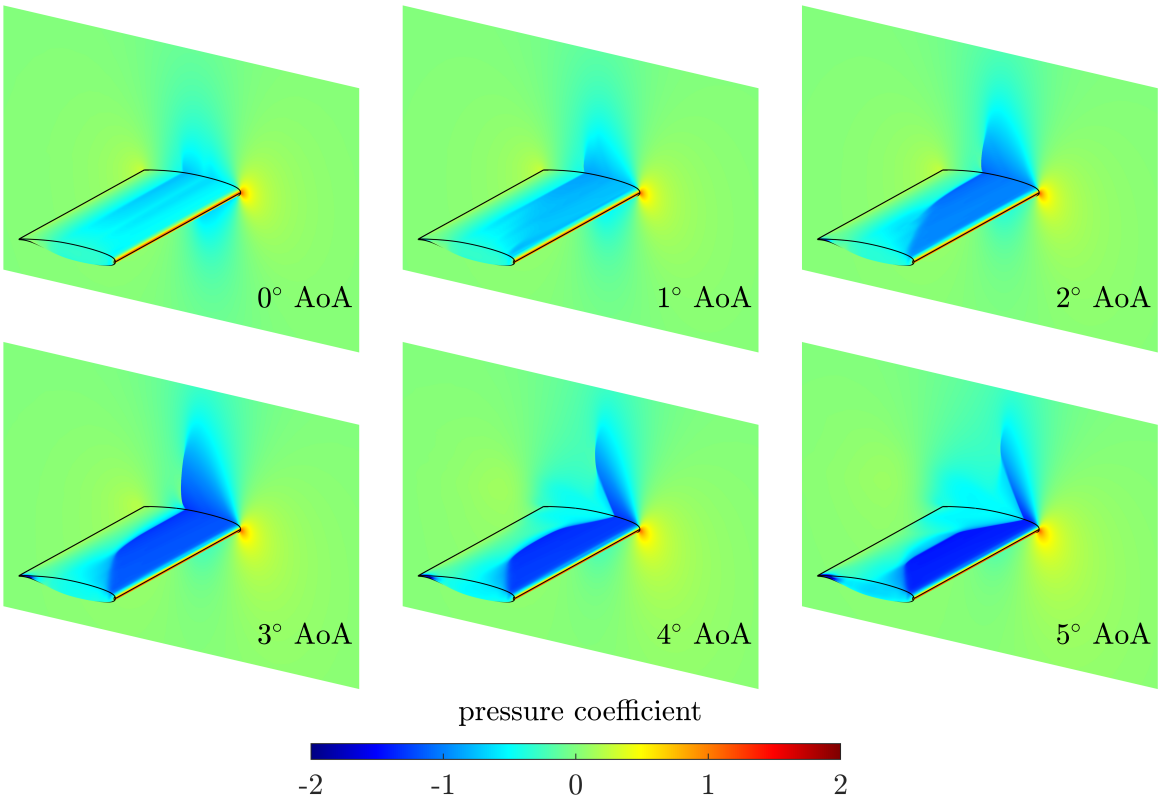

Figure 7: Static aeroelastic surface pressure coefficients.

The migration of the modal aeroelastic damping with q is shown in Fig. 9, for each AoA. Each plot overlays results from the final 10 meshes in the adaptation process of Fig. 6. The real part of the eigenvalue is shown here, as opposed to Fig. 4, and so a positive value is unstable. Similar to the convergence properties shown in Fig. 6, the convergence properties are reasonable for all AoA values below 5°; even at this AoA, the basic mechanism of the flutter plot is largely repeatable, but the damping is shallow enough that small variations in each curve lead to an outsized change in the flutter-q.

The flutter-q from each of the curves in Fig. 9 is plotted in Fig. 10, for comparison with LFD computations from the coarse and the fine manually constructed mesh (shown in Fig. 2). Also shown in the figure are flutter values extracted from time-domain simulations using the complete family of manually constructed meshes, and the experimental TDT data. The corresponding flutter frequency data are shown in Fig. 11. There are a number of interesting features of these two figures:

- Both flutter-q and flutter frequency initially drop, slightly, from 0° to 1°, and then rise up to 3°. All of the solvers and meshes are largely in agreement up to 3°, and match with the experimental data at 0° and 1°. Flutter frequency for these lower angles of attack is

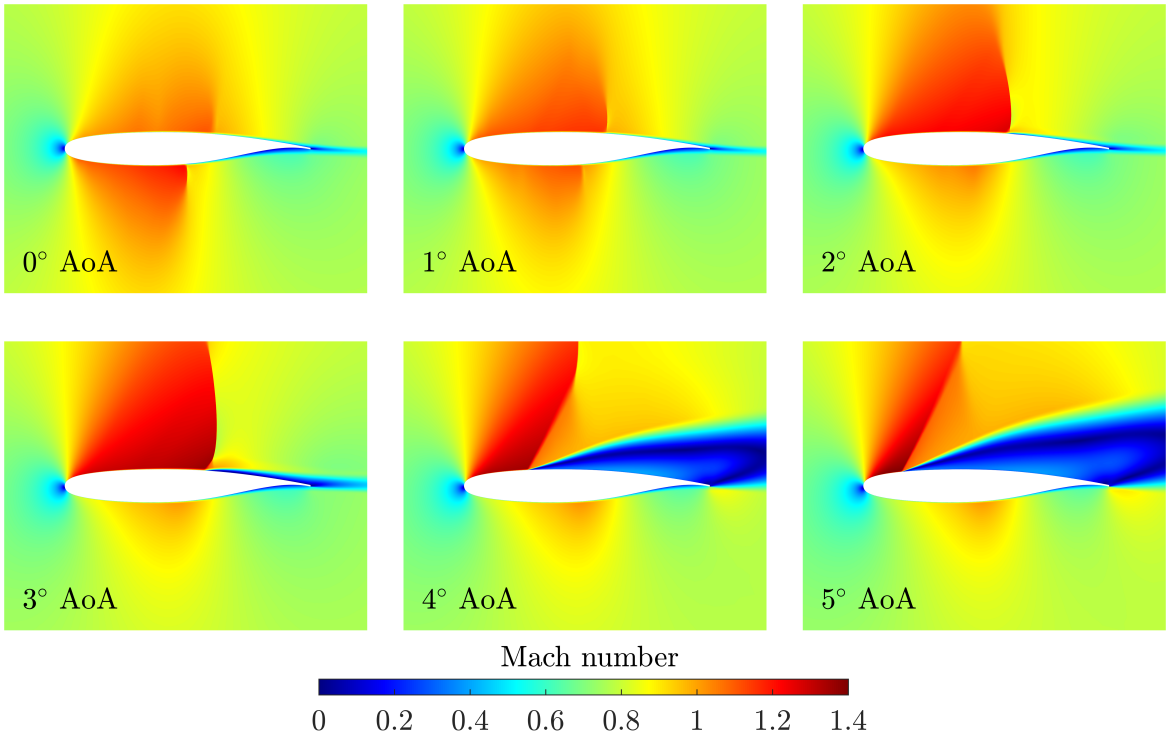

Figure 8: Static aeroelastic Mach contours along the symmetry plane.

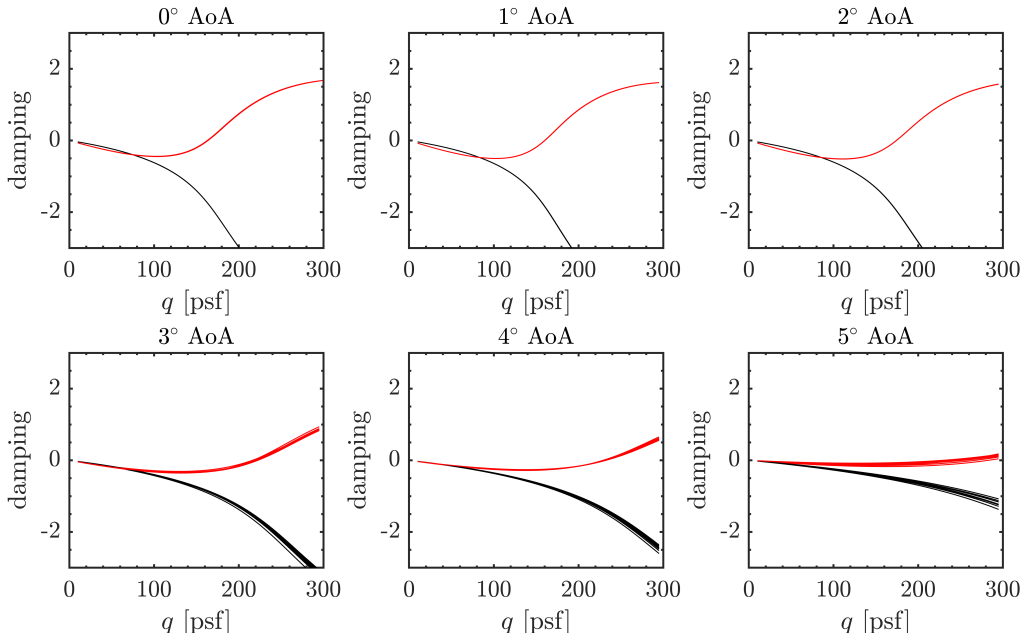

Figure 9: Variations in the aeroelastic damping migration for the final 10 meshes in the adaptation process.

nearly midway between the uncoupled plunge and pitch frequencies of the structure, as would be expected.

- Above 3°, the LFD results and the time-domain results diverge, with the LFD flutter-q increasing to nearly 250 psf (though there is a scatter of points at the highest angle attack, as discussed above), whereas the time-domain flutter-q drops with increased AoA. The generalized velocity perturbation, v, for all time-domain cases is 5; this particular value

provides a good correlation with the TDT data near 5° AoA, though as will be seen below, the flutter point above 3° AoA is very sensitive to v.

- The time-domain results are reasonably well converged at the fine and extra fine meshes. The fine mesh LFD result likewise compares well with the mesh adapted results, though the mesh adapted results are two orders of magnitude coarser than the manually constructed medium mesh. Additionally, the fine mesh LFD results are linearized about the static aeroelastic solution obtained at q=169 psf; because the flutter-q is much higher, this result is not matched point. Regardless, the result still compares well with the mesh adapted case (which *is* matched point), again indicating that matched point q issues are of secondary importance here.
- Time-domain flutter frequencies approach the uncoupled pitch frequency at higher AoA's, indicative of a pitch-dominated stall flutter mechanism. The LFD flutter frequencies also increase with increased AoA, but do not approach the pitch frequency as closely.

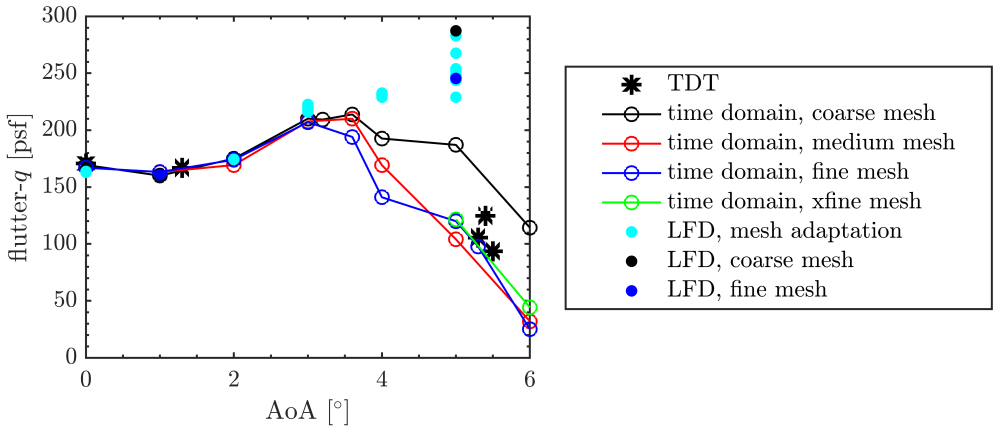

Figure 10: Variations in the computed flutter-q, compared with experimental TDT data.

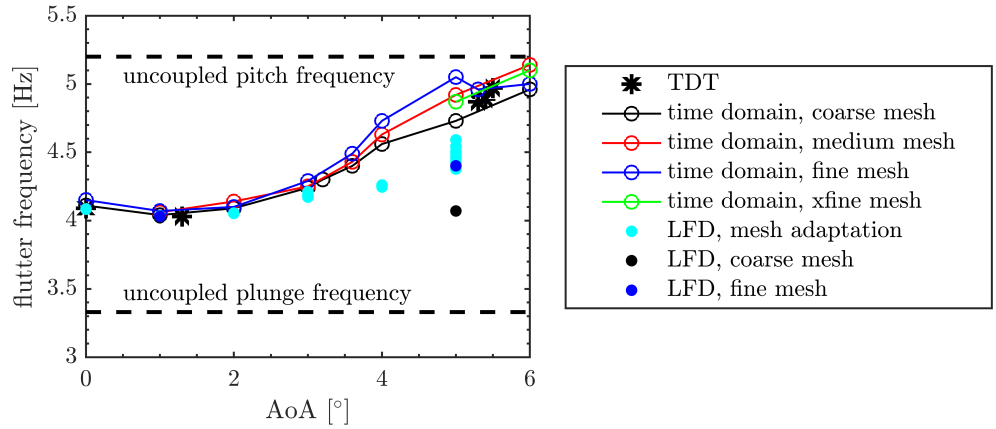

Figure 11: Variations in the computed flutter frequency, compared with experimental TDT data.

Additional time-domain results are shown in Fig. 12, using the "jig shape release" dynamic perturbation discussed above. This is done for both a DDES solver and the usual URANS solver: both cases match reasonably well to the v=5 result at 5° AoA, but DDES overpredicts the URANS flutter point at 6° AoA.

The dependency of the URANS time-domain flutter result on the value used for v is shown in

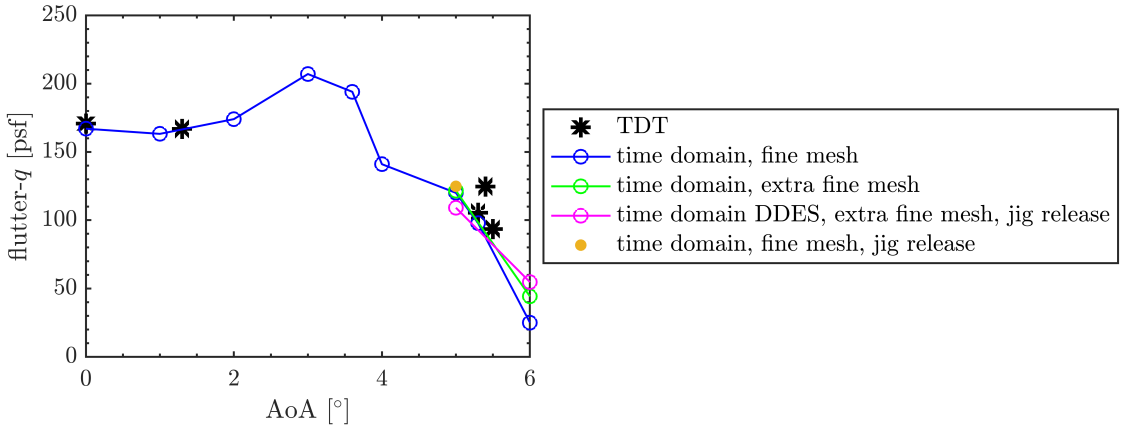

Figure 12: Variations in the computed flutter-q, compared to jig released dynamic perturbations.

Fig. 13, via the fine mesh, at 1°, 3°, 4°, and 5°. DDES flutter solutions will also likely show a strong dependence on v, but at present, this solver is too expensive to systematically map out this relationship. Stable and unstable results are noted in Fig. 13, and this mapping of points indicates a strong subcritical LCO at 4° and 5° AoA. At 5° AoA in particular, the LCO extends from the linear flutter point near 250 psf (computed with LFD, and the expected time-domain result when v is nearly 0), to unstable values near 115 psf, when v is 7.5. This subcritical LCO is weaker at 4°, and largely absent at 3° and 1° AoA: i.e. there is no strong relationship between v and flutter-q, presumably owing to the largely-attached flow at these conditions. Recall from Fig. 10, 3° is the highest AoA for which time-domain and LFD provide similar results. It can also be seen that if a different v had been used in Fig. 10, the comparison between time-domain and TDT data would be much worse at 5° AoA.

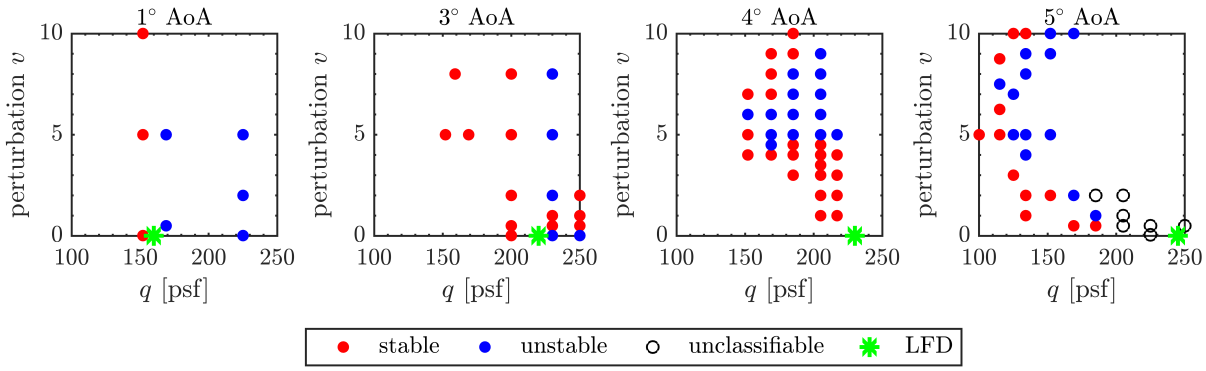

Figure 13: Subcritical limit cycle oscillations mapped out for various AoA, via the fine mesh.

Two issues are noted in Fig. 13 for time-domain results at small v. First, some stable data points are observed *above* the LFD flutter point at 3° AoA, for v values between 1 and 2. This will be discussed in more detail below, but ultimately, the reason for this behavior is not currently understood. Second, some data points at 5° are labeled as "unclassifiable", in the sense that the oscillatory modal response is not monotonically growing or decaying, as seen in the right plot of Fig. 14. The reason for this is not understood either, though it is noted to occur for high dynamic pressures, where the combination of the rigid AoA and the static twist is nearly 7° (see Fig. 6).

Perturbation dependence is further explored in Fig. 15, which shows the aeroelastic damping

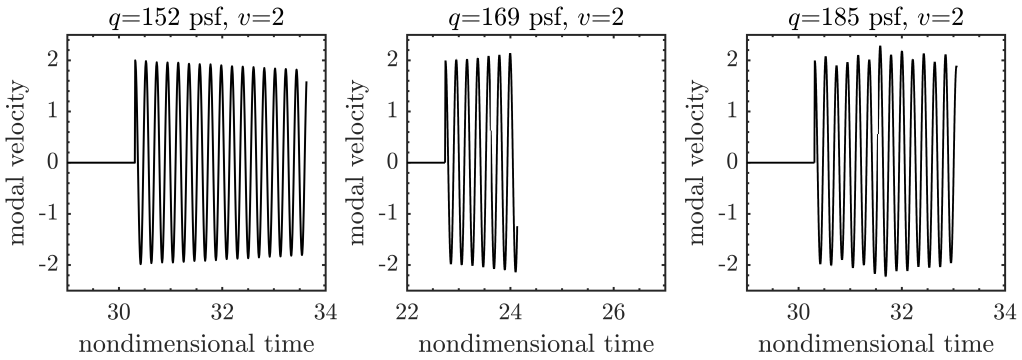

Figure 14: Aeroelastic time-domain response of the pitch mode at increasing q values.

computed as a function of v, at a fixed q and AoA. These are subcritical points, with q values chosen to be roughly 30 psf less than the LFD predicted flutter-q. A v value of 10 is the largest value considered here; above this, negative volumes are encountered in the mesh, due to excessive deformation. In theory, one could perturb the system by v=10, and let the nonlinear oscillations eventually decay to 0, but the resulting computational cost of this procedure is too high. Instead, shorter duration simulations are run (between, for example v of 10 and 8), and then a sliding window is used to estimate damping, via the matrix pencil scheme, for multiple v values between the beginning and the ending of that simulation. In Fig. 15, clustered data points of the same color, represent multiple windows within a single time-domain run.

The results of Fig. 15 largely echo the LCO results of Fig. 13, with a very sensitive relationship between v and damping for AoA's of 4° and 5°. At 3°, low v values lead to unexpected damping variations, as above: further work is needed to better understand this trend. Finally, while the 1° data are mostly insensitive to v, owing to the weaker nonlinearities, the spread in the estimated damping (via the matrix pencil tool) is larger, and the reason for this is presently unclear. This is as opposed to the higher AoA values, where the single pitch mode dominates.

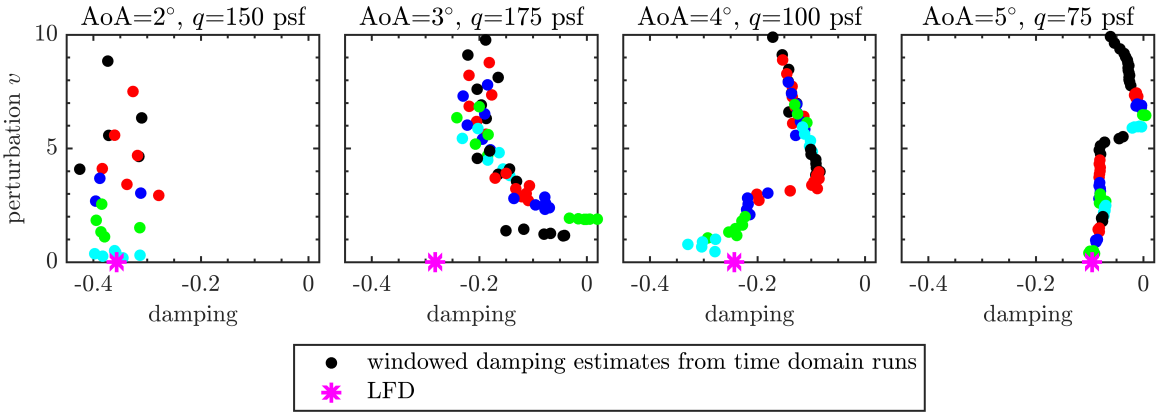

Figure 15: Preflutter damping computations from both time and frequency-domain solvers. Different colored time-domain symbols are from the same simulation, but using a sliding windows for the matrix pencil tool.

Next, the computed flow physics are used to explain the sensitive relationship between v and damping at higher AoA's. Oscillatory pressure coefficients are shown in Fig. 16 at four snapshots through the wing pitching cycle at the steady AoA of 4°. The contour in these figures is the difference between the instantaneous time dependent pressure coefficient and the static

aeroelastic pressure coefficient, normalized by the perturbation size, v. Four v values are shown in the figure: 6.3, 3.6, 1.8, and 0.4, chosen because they correspond to distinct damping regions in the 4° data of Fig. 15. It is noted that the airfoil drawings in the figure are not to scale, but only to give a sense of the snapshot motion. The four v values correspond to physical pitch amplitudes of 3.1°, 2.2°, 1.7°, and 1.24°.

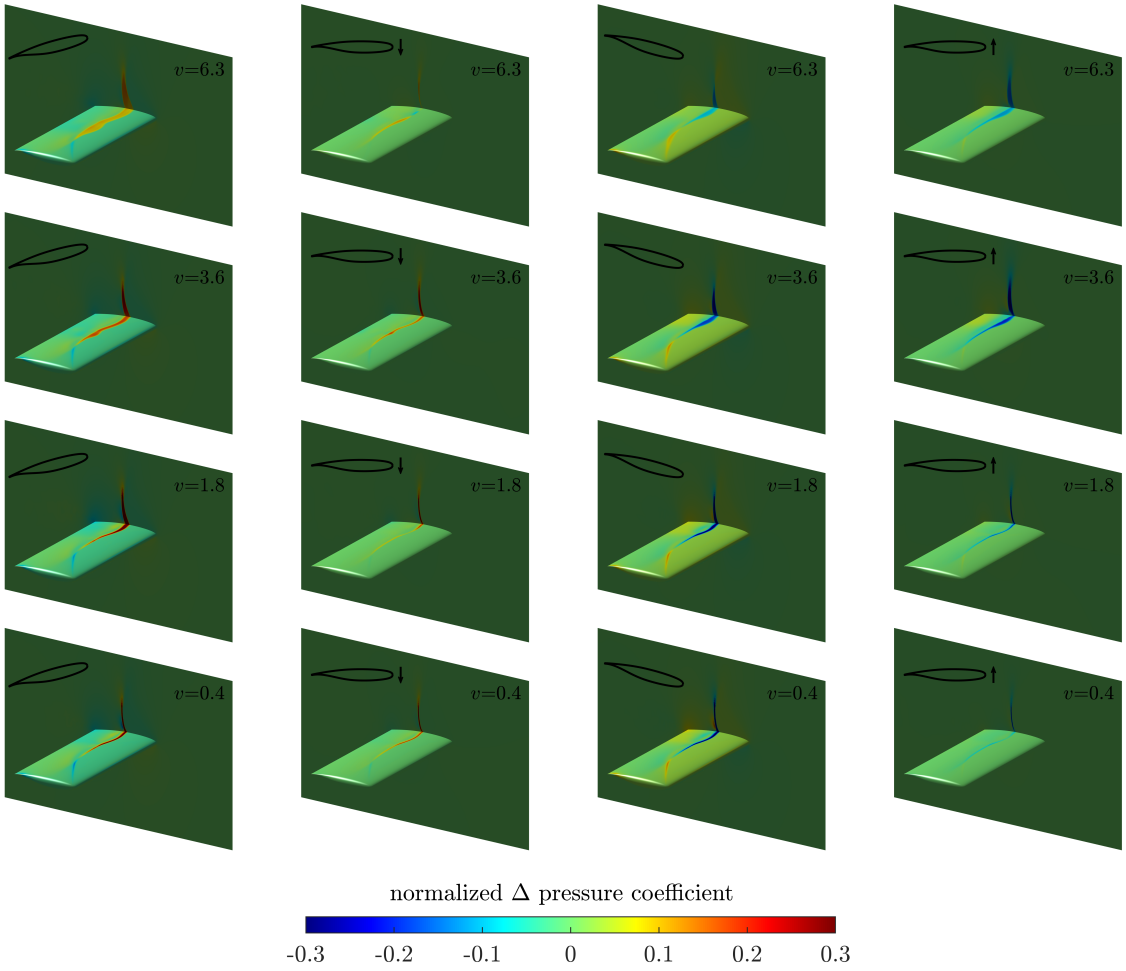

Figure 16: Normalized oscillatory pressure coefficients computed at 4° AoA, for four snapshots during the aeroelastic cycle.

Because the oscillatory pressure coefficients are normalized by the perturbation v, differences in pressure between different v values directly reflect nonlinear amplitude dependencies (largely driven by flow separation). The pressure contours at the lowest v level should be similar to those obtained with the LFD solver (though this comparison is not made here), and is characterized by thin bands traveling down and above the wing, along the shock location. Positive oscillatory pressures indicate that the shock has increased in strength (seen for wing pitch up in Fig. 16), and vice versa. At higher levels of v, the bands of oscillatory pressure widen, blur, and decrease in amplitude, due to finite motion of the shock in response to fluttering motion. The key exception to this trend is through the upstroke of the pitching motion (right column of the figure), where the negative oscillatory pressure is largest at v=3.6 (i.e., the shock is attenuated), potentially correlating with the rapid destabilization of the aeroelastic system at 4° AoA in Fig. 15 at this same v level.

6 CONCLUSIONS AND FUTURE PLANS

This paper presents an extension of the recent 3rd Aeroelastic Prediction Workshop. That workshop considered transonic flutter of the Benchmark Supercritical Wing, at 5° AoA and Mach 0.8, a case which is characterized by large regions of separated flow. Workshop participants predicted a wide range of flutter-q values, owing in part to the weak and shallow flutter mechanism, which is very sensitive to various modeling options.

A deeper insight into the key aeroelastic physics of this AePW case is currently lacking, due to several reasons. First, the only experimental data available for this case is the flutter-q itself, rather than on or off body flow quantities. Second, only the single 5° AoA Mach 0.8 case was considered: this case is very challenging for modern aeroelastic solvers. Looking instead at a range of AoA (or Mach) values with increased transonic effects, may improve our understanding of why the solvers gradually begin to struggle (provided there is suitable experimental data across this range also). Third, the 5° AoA Mach 0.8 flutter case is very sensitive to the perturbation size, which had not been specified as a controlled input to the workshop participants. This paper considers these latter two effects by modeling the aeroelasticity across an AoA-sweep with a variety of different solvers and also sweeping through different perturbation sizes to map out the subcritical limit cycle oscillation.

While the ability to control the perturbation size in the TDT is not readily available, future efforts to retest the BSCW in the TDT will attempt to obtain data (including on and off body flow quantities) across the entire AoA-sweep at Mach 0.8. Currently, data exists at 0°, 1°, and 5° AoA, but the key AoA of 3° (where the linearized frequency-domain solvers and the time-domain solvers diverge) is unfortunately missing from the dataset. The likely reason for this omission is that the flutter dynamic pressure at 3° AoA is too high (estimated above 200 psf above), and the static stresses in the PAPA mechanism no longer satisfy the required TDT safety margins.

The future retest would likely encounter this same issue; a potential solution is to test at a slightly lower Mach value, which may show the same basic flutter trends (a peak in flutter-q near 3°, followed by a drop), but a shallower, and therefore attainable, flutter peak. Preliminary results at lower Mach values are shown in Fig. 17, via the mesh adapted LFD tool, where the vertical bars reflect the variation in the flutter-q across the final 10 meshes. The figure does in fact show that a slight drop to Mach 0.77 can bring the 3° flutter point down considerably, but otherwise preserves the basic trend seen at Mach 0.8. The LFD flutter curves in the figure continue to rise beyond 3°, though the expectation is that finite amplitude effects (which are not captured by the LFD solver) will cause the flutter-q to drop at higher AoA's in the TDT.

7 REFERENCES

[1] Edwards, J., "Calculated Viscous and Scale Effects on Transonic Aeroelasticity," *Journal of Aircraft*, Vol. 45, No. 6, pp. 1863-1871, 2008.

[2] Bendiksen, O., "Review of Unsteady Transonic Aerodynamics: Theory and Applications," *Progress in Aerospace Sciences*, Vol. 47, No. 2, pp. 135-167, 2011.

[3] Bennett, R., "Test Cases for Flutter of the Benchmark Models Rectangular Wings on the Pitch and Plunge Apparatus," Defense Technical Information Center TR ADPO10713, Fort Belvoir, VA, 2000.

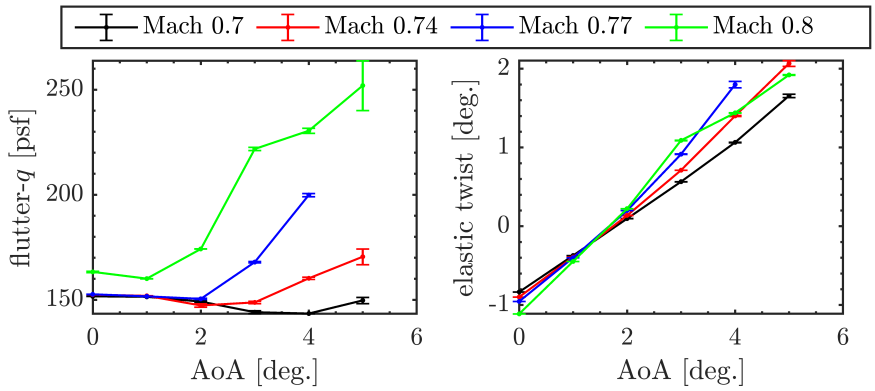

Figure 17: LFD-based mesh refinement flutter prediction at lower Mach numbers.

[4] Chwalowski, P., et al. "Flutter Prediction Report in support of the High Angle Working Group at the Third Aeroelastic Predictions Workshop" *AIAA Scitech Forum*, AIAA Paper 2024-0418.

[5] Chwalowski, P., Massey, S., Jacobson, K., Silva, W., Stanford, B., "Progress on Transonic Flutter and Shock Buffet Computations in Support of the Third Aeroelastic Prediction Workshop" *AIAA Scitech Forum*, 2022.

[6] Biedron, R., Carlson, J., Derlaga, J., Gnoffo, P., Hammond, D., Jacobson, K., Jones, W., Kleb, B., Lee-Rausch, E., Nielsen, E., Park, M., Rumsey, C., Thomas, J., Thompson, K., Walden, A., Wang, L., Wood, W., "FUN3D Manual: 13.7," NASA TM-2020-5010139.

[7] Dansberry, B., Durham, M., Bennet, R., Rivera, J., Silva, W., Wieseman, C., Turnock, D., "Experimental Unsteady Pressures at Flutter on the Supercritical Wing Benchmark Model," AIAA Paper 93-1592-CP, 1993.

[8] Bartels, R., Rumsey, C., Biedron, R., "CFL3D Version 6.4 - General Usage and Aeroelastic Analysis," NASA TM 2006-214301.

[9] Biedron, R., Thomas, J., "Recent Enhancements To The FUN3D Flow Solver For Moving-Mesh Applications," AIAA Paper 2009-1360.

[10] Vatsa, V., Lockard, D., Spalart, P., "Grid Sensitivity of SA-Based Delayed-Detached-Eddy-Simulation Models for Blunt-Body Flows," *AIAA Journal*, Vol. 55, No. 8, pp. 2842–2847, 2017.

[11] Jacobson, K., Kiviaho, J., Kennedy, G., Smith, M., "Evaluation of Time-Domain Damping Identification Methods for Flutter-Constrained Optimization," *Journal of Fluids and Structures*, Vol. 87, pp. 174-188, 2019.

[12] Golla, T., Kennedy, G., Riso, C., "A Sliding-Window Matrix Pencil Method for Aeroelastic Design Optimization with Limit-Cycle Oscillation Constraints," AIAA Paper 2024-2413.

[13] Jacobson, K., Stanford, B., Wood, S., Anderson, W., "Frequency-Domain Flutter Analysis and Sensitivities with Stabilized Finite Elements," *AIAA SciTech Forum*, Orlando, FL, January 6-10, 2020.

[14] Anderson, W., Newman, J., Karman, S., "Stabilized Finite Elements in FUN3D," *Journal of Aircraft*, Vol. 55, No. 2, pp. 696-714, 2017.

[15] van Zyl, L., Maserumule, M., "Divergence and the p-k Flutter Equation," *Journal of Aircraft*, Vol. 38, No. 3, pp. 584-586, 2001, https://doi.org/10.2514/2.2805.

[16] Jacobson, K., Stanford, B., Kiviaho, J., Ozoroski, T., Park, M., Chwalowski, P., "Multiscale Mesh Adaptation for Transonic Aeroelastic Flutter Problems," *AIAA Aviation Forum*, virtual event, 2021.

[17] Kleb, B., Park, M., Wood, W., Bibb, K., Thompson, K., Gomez, R., Tesch, S., "Sketch-to-Solution: An Exploration of Viscous CFD with Automatic Grids," *AIAA Aviation Forum*, Dallas, TX, June 17-21, 2019.

[18] Balan, A., Park, M., Anderson, W., Kamenetskiy, D., Krakos, J., Michal, T., Alauzet, F., "Verification of Anisotropic Mesh Adaptation for RANS Simulations over a ONERA M6 Wing," *AIAA Journal*, Vol. 58, No. 4, pp. 1550-1565, 2020.

[19] Loseille, A., Dervieux, A., Frey, P., Alauzet, F., "Achievement of Global Second Order Mesh Convergence for Discontinuous Flows with Adapted Unstructured Meshes," *AIAA Computational Fluid Dynamics Conference*, Miami, Florida, 2007.

[20] Alauzet, F., George, P., Mohammadi, B., Frey, P., Borouchaki, H., "Transient Fixed Point-Based Unstructured Mesh Adaptation," *International Journal for Numerical Methods in Fluids*, Vol. 43, No. 6-7, pp. 729–745, 2003.